Invited Paper

Tumors in murine brains studied by grating-based phase contrast microtomography

Georg Schulz[a], Marco Dominietto[a,b], Zsofia Kovacs[c,d], Rüdiger Schmitz[a], Simone E. Hieber[a], Peter Thalmann[a], Felix Beckmann[e], and Bert Müller[a]

[a]Biomaterials Science Center, University of Basel, 4031 Basel, Switzerland;
[b]Institute for Biomedical Engineering, ETH Zürich, 8092 Zürich, Switzerland;
[c]Center for MR-Research, University Children's Hospital Zürich, 8032 Zürich, Switzerland;
[d]Oncology Department, University Children's Hospital Zürich, 8032 Zürich, Switzerland;
[e]Institute of Materials Research, Helmholtz-Zentrum 21502 Geesthacht, Germany

ABSTRACT

Angiogenesis, i.e. the formation of vessels, is one of the key processes during tumor development. The newly formed vessels transport oxygen and nutrients from the healthy tissue to the tumor and gives tumor cells the possibility to replicate. The principle of anti-angiogenic therapy is to block angiogenic process in order to stop tumor growth. The aim of the present study is the investigation of murine glioma vascular architecture at early (7 days), intermediate (10 and 15 days) and late (23 days) stage of growth by means of grating-based phase contrast microtomography. We demonstrate that this technique yields premium contrast between healthy and cancerous parts of murine brain tissues.

Keywords: Synchrotron radiation-based microtomography, murine brain tumors, tumor growth, grating interferometry

1. INTRODUCTION

High-grade glioma is a very aggressive tumor with an average survival rate between 12 and 14 months after diagnosis despite treatment with existing therapies. The survival rate after one year is approximately 30 %, and after two years is only 14 % [1]. It originates from a mutation of glial cells, which are present in the brain and in the spine. The glial cells have important functions including the support and protection of the neurons by providing nutrients and oxygen, destroying pathogens and forming myelin.

Nowadays the standard treatment of glioma consists of a combination of a surgical resection of the tumor mass, adjuvant chemotheraphy and radiotherapy treatment of the tumor bed and surgical margins. Moreover, anti-angiogenic treatments following radiotherapy are under evaluation in clinical trials.

Glioma tumor is characterized by high proliferation rate [2], which means cell replication of around 2 to 25 times faster than normal cells [3], high angiogenic rate and tissue heterogeneity. These features give the tumor mass the ability to microscopically invade surrounding tissues making the complete surgical resection almost impossible. Such invasion is responsible for the development of tumor recurrences and secondary tumor formations that make this kind of tumor almost lethal.

Angiogenesis is a crucial step in tumor development since it promotes the formation of a vascular structure which delivers oxygen and nutrients needed for tumor cells replication and tissue formation [4]. On the one hand, this makes the tumor more aggressive, on the other hand it can be used as a target for therapy. The goal of anti-angiogenic therapy consists of blocking angiogenic factors of vessels in order to prevent nutrients delivery, which in turn avoids cell replications.

Current anti-angiogenic drugs target specific growing factors, as VEGF (Vascular Endothelial Growth Factor) which is mainly responsible for the formation of capillaries and angiopoietins which are required for the formation

Further author information: (Send correspondence to G.S.)
E-mail: georg.schulz@unibas.ch, Telephone: +41 61 265 9125, Fax: +41 61 265 9699; www.bmc.unibas.ch

Developments in X-Ray Tomography IX, edited by Stuart R. Stock, Proc. of SPIE Vol. 9212,
92120Q · © 2014 SPIE · CCC code: 0277-786X/14/$18 · doi: 10.1117/12.2060544

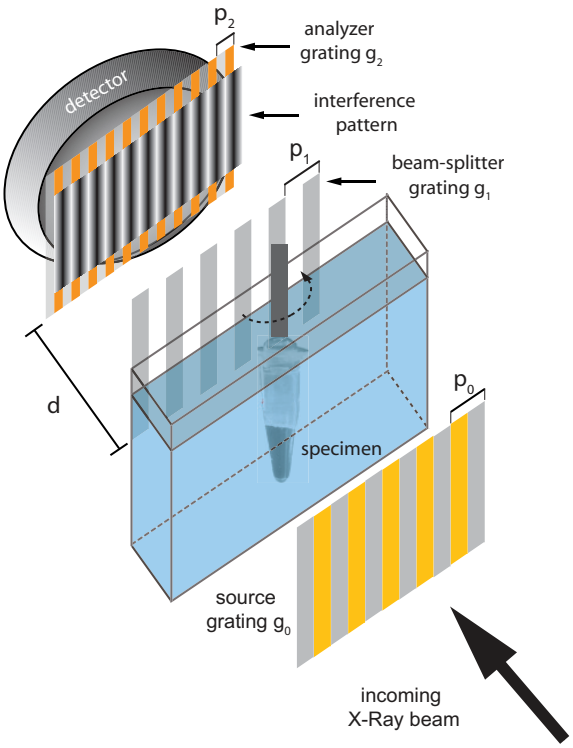

Figure 1. Schematic of the interferometer consisted of three gratings: source grating g_0, beam-splitter grating g_1 and analyzer grating g_2. During the measurements the specimen is located in a water tank.

and maturation of larger vessels [5]. Clearly, the type and amount of administered drug is related to the quantity of capillaries and large vessels. In this regards, the detailed characterization of vascular architecture is the first critical point to determine the optimal anti-angiogenic treatment.

In order to segment the vessel tree from the surrounded soft tissue an imaging technique with an adequate contrast between blood vessels and the surrounded parts and a spatial resolution on the level of the size of capillaries is required. Magnetic resonance microscopy (MRM) operating at high magnetic field (around 9 T) is a non-destructive 3D imaging technique with high contrast within soft tissues but with limited spatial resolution of around one magnitudes larger than that of the smallest capillaries. Synchrotron radiation-based micro computed tomography (SRμCT) in absorption contrast provides the required spatial resolution but shows weak contrast within soft tissues if no contrast agent is used. On the other side corrosion casts in combination with absorption contrast SRμCT can be used for the visualization of the vessel trees [6]. The problem of staining the blood vessels with contrast agent or during the fabrication of the corrosion casts is that the contrast agent or the polymer resin would exit the vessel tree in the necrotic part of the tumor where the blood vessel walls are damaged [7]. Therefore, SRμCT experiments were carried out in phase contrast mode which is based on the phase shifts of X-ray waves penetrating the specimen [8]. Today different operating modes are existent. An overview of the main X-ray phase contrast approaches can be found in literature [9]. During the present study grating interferometry [10–13] was used.

The goal of this work is to provide a characterization of the vascular tumor network in case of glioma tumor growing in murine brain.

2. MATERIALS AND METHODS

2.1 In-vivo experiments and specimen preparation

Four female B6 (Cg)-Tyrc-2J/J mice weighting 24-26 g (The Jacksons Laboratory, Bar Harbor, ME, USA) have been used for all experiments. A suspension of 2×10^5 GL261 murine glioma cells have been orthotopically

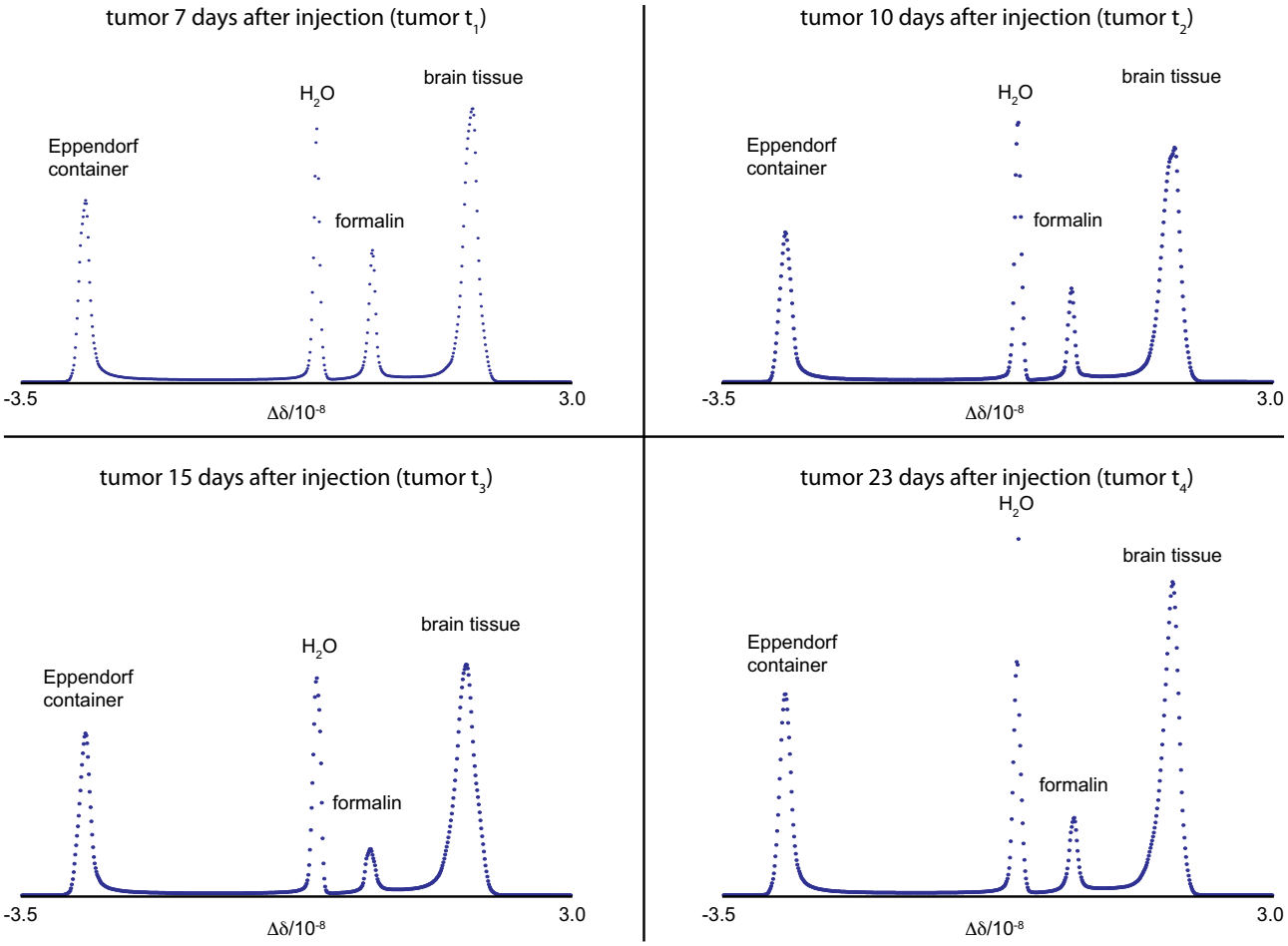

Figure 2. Histograms of the four data sets at the selected stages of tumor growth showing the whole scale range of the $\Delta\delta$ values.

injected into the right brain cortex using a stereotactic frame. Magnetic Resonance Images (MRI) have been acquired at day 7 (specimen termed t_1), 10 (termed t_2), 15 (termed t_3) and 23 (termed t_4) following tumor inoculations in order to assess tumor dimensions. After MRI experiment, a single mouse has been sacrificed for each day of measurement. Brain samples has been removed after perfusion with 4 % paraformaldehyde (PFA) and stored in an Eppendorf container filled with PFA. Please note, that formalin fixation induces global and local changes in the brain tissue. The global volume shrinkage between a human brain inside the cranium and after extraction and formalin fixation is shown to be in the range of 3.5 % [14]. In total, we obtained four brain samples with four tumors at different stages. These tumors measures 1 mm (t_1), 2 mm (t_2), 3 mm, (t_3) and 4 mm (t_4) in diameter.

2.2 Grating-based phase contrast

The phase contrast experiments were carried out at the wiggler beamline W2 (HASYLAB, DESY, Hamburg, Germany) operated by Helmholtz Research Center Geesthacht [15]. The grating interferometer installed there [16] consisted of three gratings because of the horizontal source size of 1.7 mm (see Fig. 1). Using a double-crystal Si(111)-monochromator in Laue geometry the photon energy of 23 keV was selected. To image the complete tumors one height step with a field of view of 4.5 mm height and 14.4 mm width was adequate. The absorbing grating g_0 (source grating with periodicity of $p_0 = 22.29$ μm) and beam-splitter grating g_1 with periodicity of $p_1 = 4.33$ μm were fabricated at the Paul Scherrer Institut, Villigen, Switzerland involving photolithography, deep etching into silicon and for grating g_0 electroplating of gold [17]. The analyzer grating g_2 (Karlsruhe

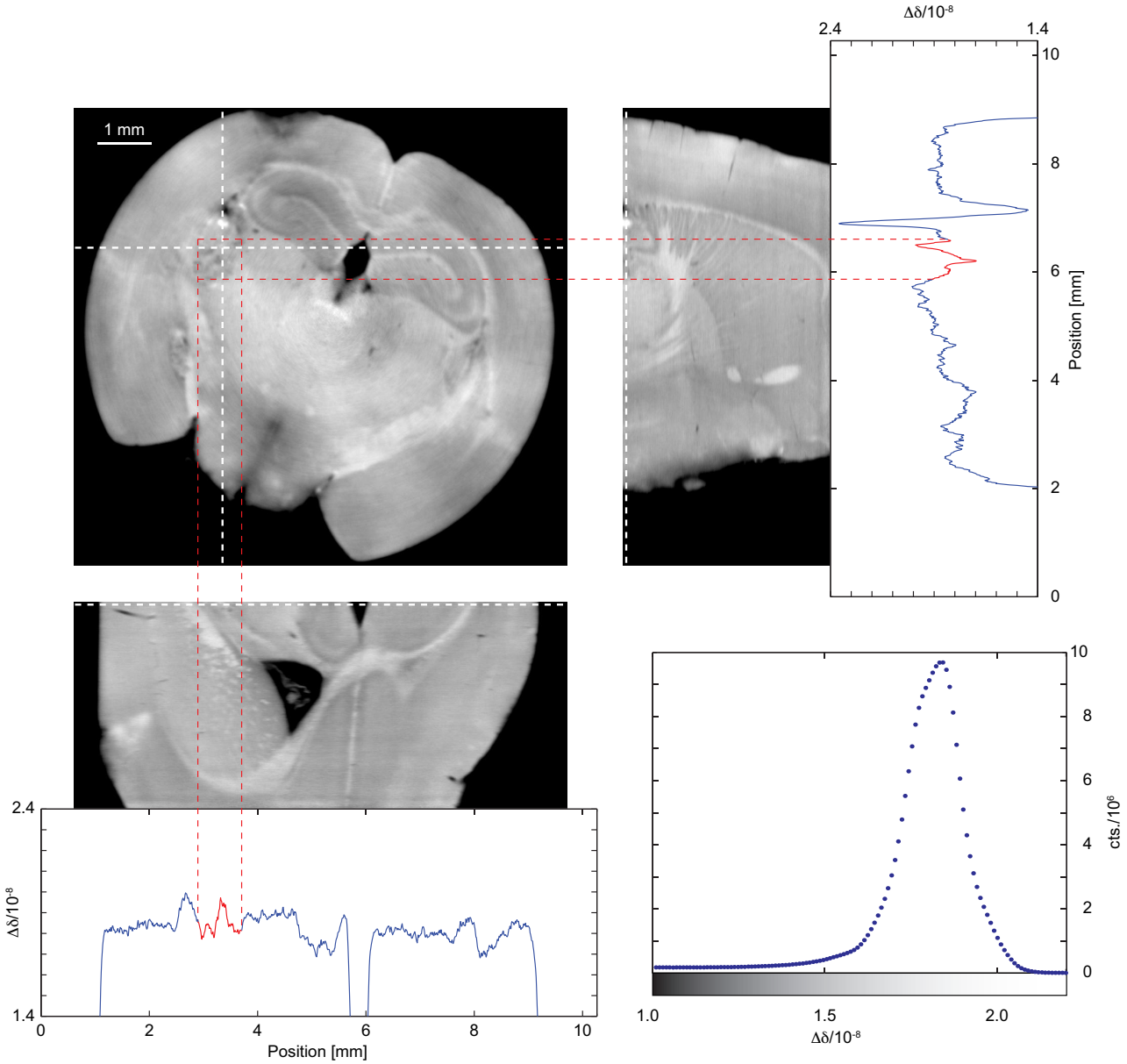

Figure 3. Orthogonal reconstructed slices through the mouse brain showing the tumor t_1. The white dashed lines indicate the positions of the line plots through the slices. The gray scale values of the images are accordant to the gray scale bar below the histogram which shows the brain tissue peak.

Institute of Technology, Eggenstein-Leopoldshafen, Germany) [18] consisted of lines of gold with a periodicity of $p_2 = 2.40$ μm. With a distance between source and grating g_0 of 45 m and a distance between the gratings of $d = 322$ mm, the set up corresponded to the 7^{th} fractional Talbot order. During the measurements, the Eppendorf container was placed in a water tank with parallel polymethylmethacrylate plates in order to minimize artefacts due to X-ray phase curvature induced by a conical container-air interface. This water tank was located around 10 cm upstream of grating g_1. The detector consisted of a luminescence screen, a Nikon lens, and a Finger Lake Instruments PLO9000 CCD camera with an active area of 3056 $\times$ 3056 pixels and a real pixel size of 12 μm. The effective pixel size during the experiments was 4.7 μm and the spatial resolution of 8.9 μm. It was placed approximately 5 cm downstream of the analyzer grating. Projection radiographs were taken in 801 steps

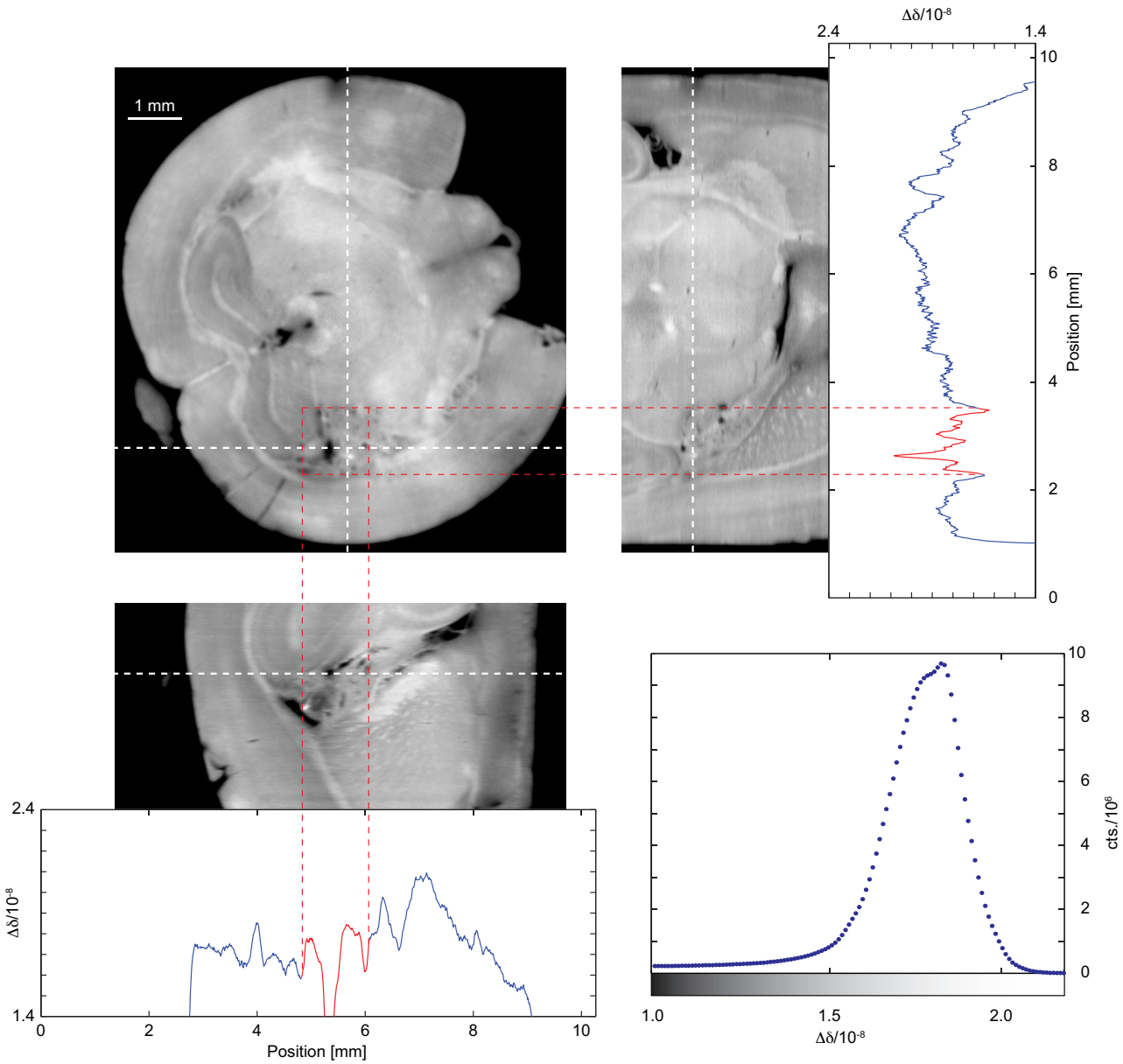

Figure 4. Orthogonal reconstructed slices through the mouse brain showing the tumor t_2. The white dashed lines indicate the positions of the line plots through the slices. The gray scale values of the images are accordant to the gray scale bar below the histogram which shows the brain tissue peak.

over a range of 360°. At each projection angle, eight phase-stepping images were taken over two periods of the interference pattern.

2.3 Data treatment

In order to improve the contrast of the data sets the intensity images were binned twofold [19]. Before reconstruction, each set of five images acquired during the phase-stepping procedure were processed using Fourier analysis and sinograms were generated which were corrected simply by a line-by-line subtraction of the mean values [20]. After the generation of the sinograms a modified filter kernel (Hilbert transform) in combination with standard back-projection algorithm [13,21,22] was used for the reconstruction of the data sets. All the data

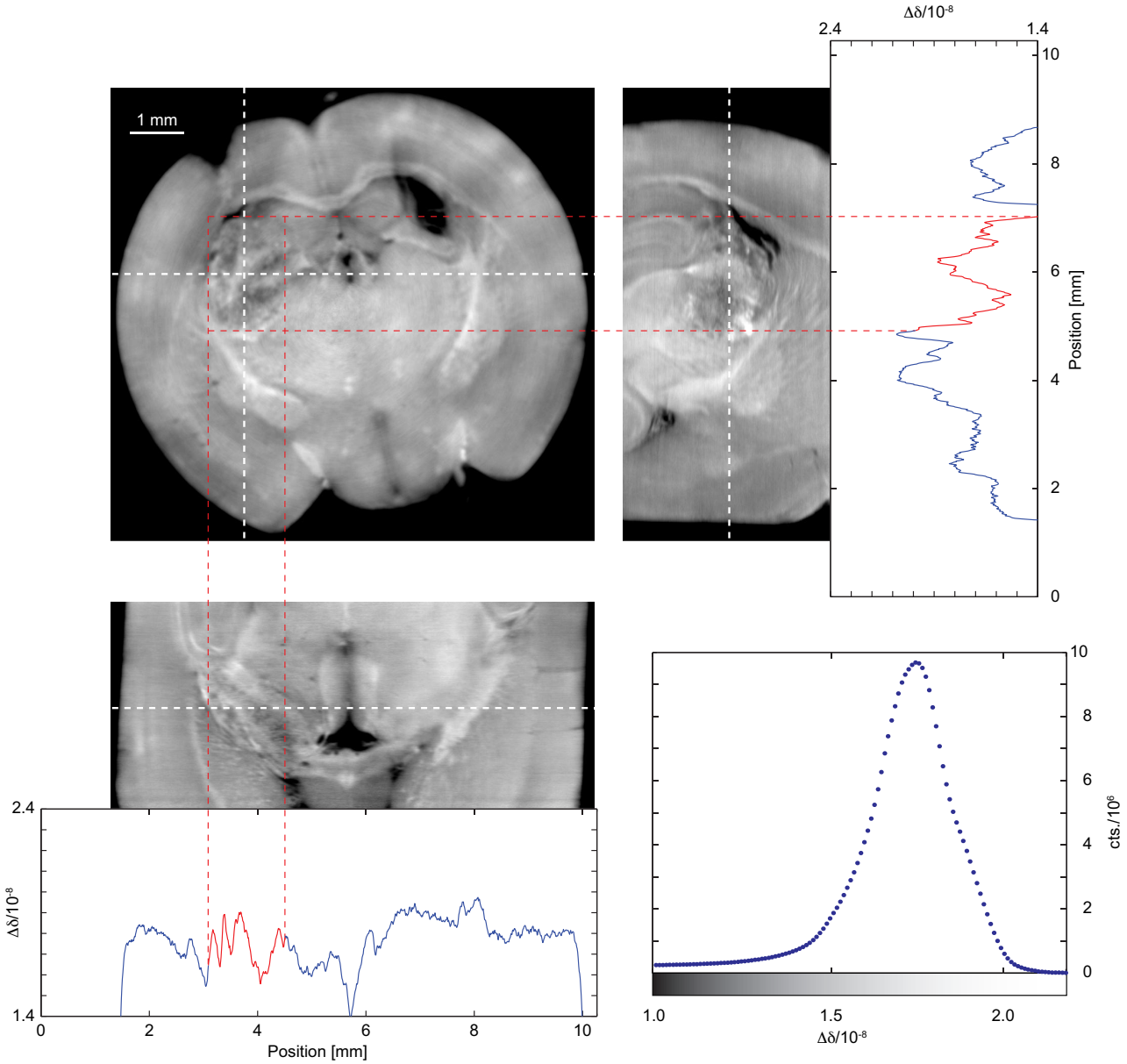

Figure 5. Orthogonal reconstructed slices through the mouse brain showing the tumor t_3. The white dashed lines indicate the positions of the line plots through the slices. The gray scale values of the images are accordant to the gray scale bar below the histogram which shows the brain tissue peak.

treatment concerning processing and reconstruction of the data were performed using Matlab 8.3 (MathWorks, Natick, USA).

For the intensity-based segmentation of the data and the 3D renderings VGStudio MAX 2.1 (Volume Graphics GmbH, Heidelberg, Germany) was used.

For the blood vessels segmentation the 3D data were processed using a Vessel Enhancing Diffusions (VED) filter [23,24] as implemented in Matlab 8.3 (MathWorks, Natick, USA). The filter employs an anisotropic diffusion scheme governed by a smoothed version of Frangis vesselness measure to enhance tubular, vessel-like structures and suppress noise. The thresholds controlling the sensitivity of the VED filter towards plane-, blob- and vessel-like structures, typically denoted by α, β and γ respectively, are selected based on visual inspection of the original

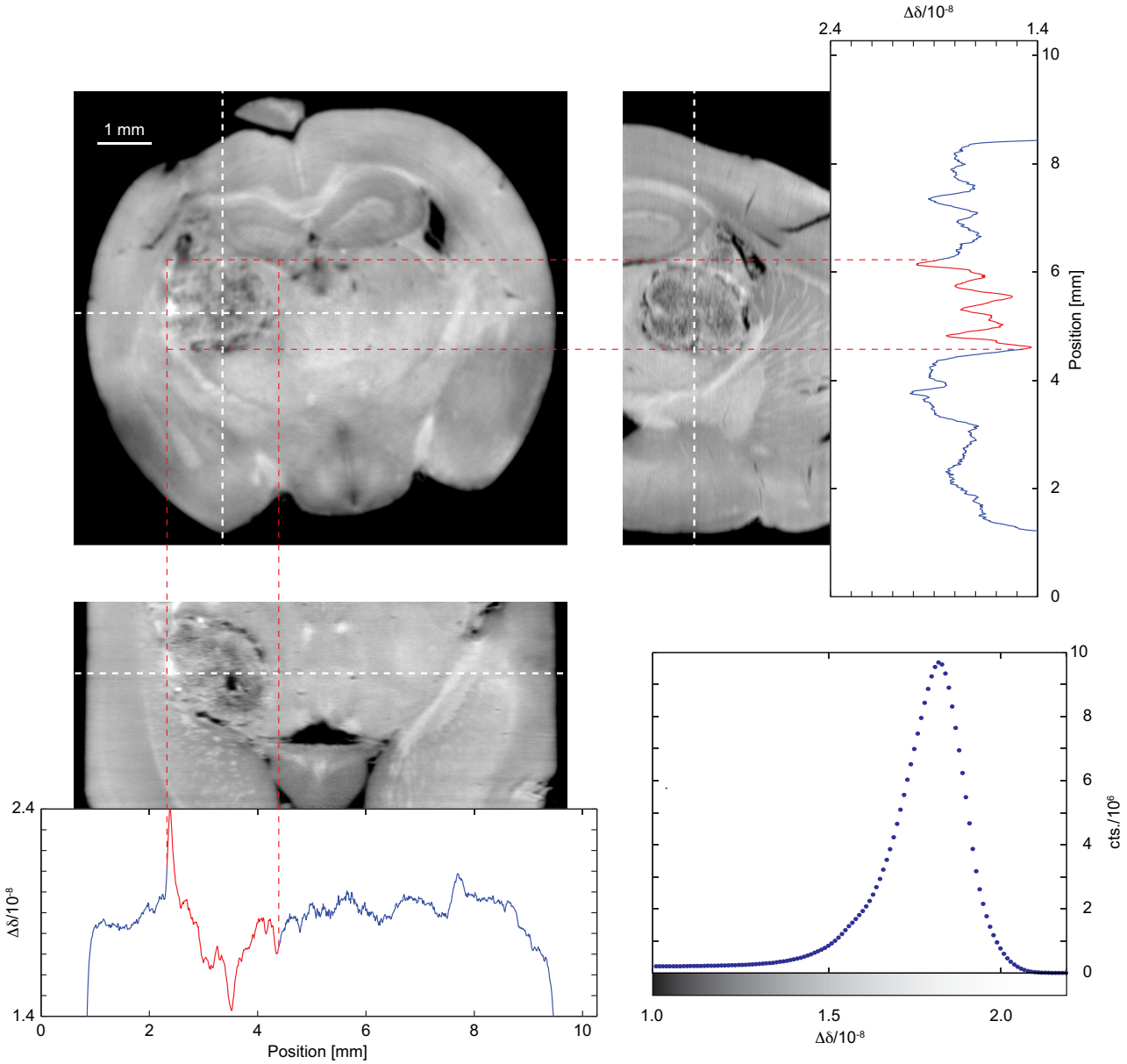

Figure 6. Orthogonal reconstructed slices through the mouse brain showing the tumor t_4. The white dashed lines indicate the positions of the line plots through the slices. The gray scale values of the images are accordant to the gray scale bar below the histogram which shows the brain tissue peak.

and vessel-enhanced images. Moreover, the filter is sensitive to a range of preselected vessel radii selecting the scale σ which leads to the largest response.

Following the VED filtering step, the data are binarised by an appropriate threshold. In order to obtain a faithful and well-connected image of the vessel tree, the threshold is chosen to be as low as possible, with the resulting noise being removed afterwards by discarding everything but only the largest connected components of the 3D data set.

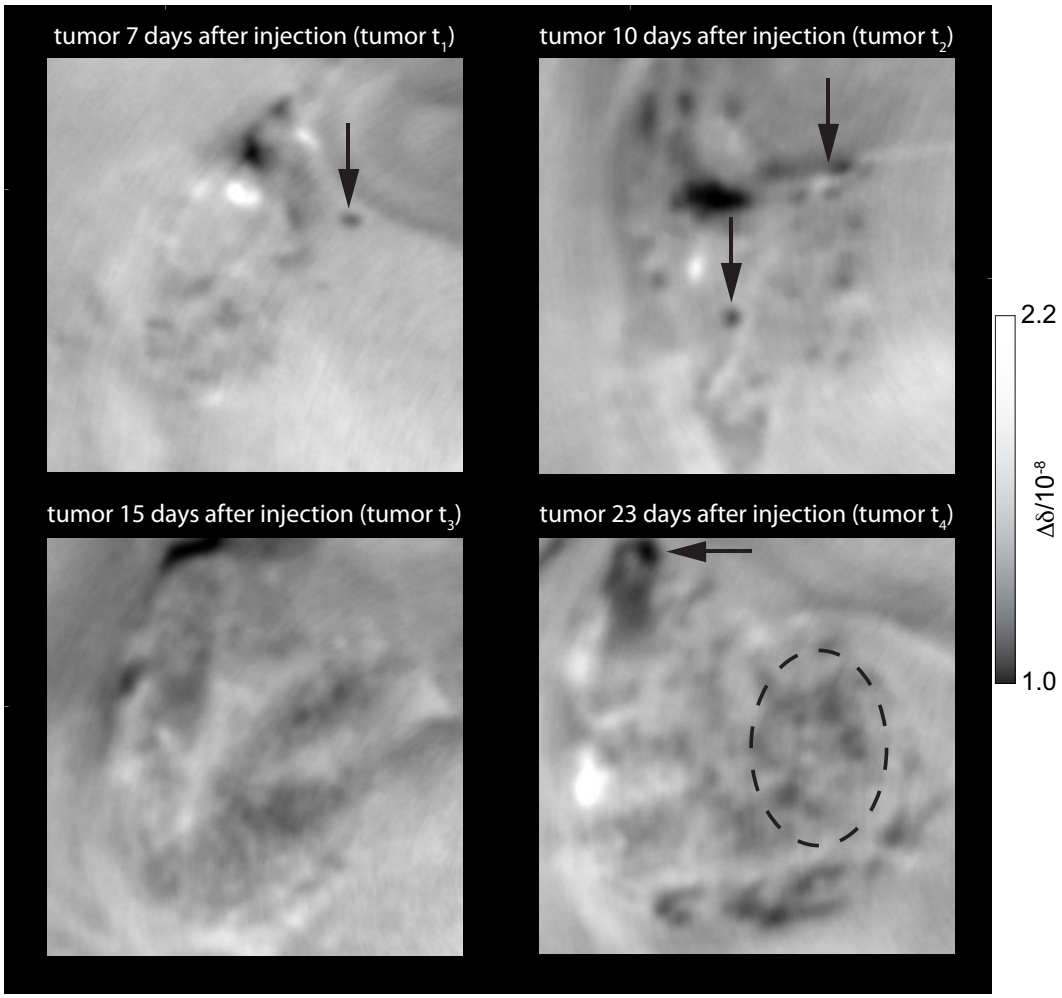

Figure 7. Zooms into slices of the four brains shown in Figs. 3, 4, 5 and 6 displaying the morphology of the tumor at four selected stages of growth.

3. RESULTS AND DISCUSSION

3.1 Identification of cancerous tissue

The histograms in Fig. 2 containing the gray values of the data consist of four separated peaks identified as Eppendorf container, water, formalin and the brain tissue. The enlarged histograms in Figs. 3, 4, 5 and 6 bottom right show only the peaks related to the brain tissue. On the left side of these brain peaks a shoulder can be identified which seems to slightly go up with the age of the tumor. Therefore, tissues with $\Delta\delta$-values of this shoulder appear to be cancerous tissues.

Figures 3, 4, 5 and 6 show slices of the four brains from the three orthogonal directions. The gray values correspond to the decrement of the real part of the refractive index relatively to water. Besides the possible identification of anatomical structures in the murine brain also the tumors can easily be seperated from healthy tissues. Line plots through the tumorous parts of the images show that the gray values of the tumorous tissues are slightly lower (red line) compared to the surrounded healthy tissues (blue line). These four figures drastically show how fast the tumors are growing. In between Fig. 3 (tumor t_1) and Fig. 6 (tumor t_4) there is only a period of around two weeks.

Enlarged regions of the tumerous parts are shown in Fig. 7. The figure illustrates the first differences between the tumors at the selected stages of growth. Whereas at the beginning, the tumors seem to have more

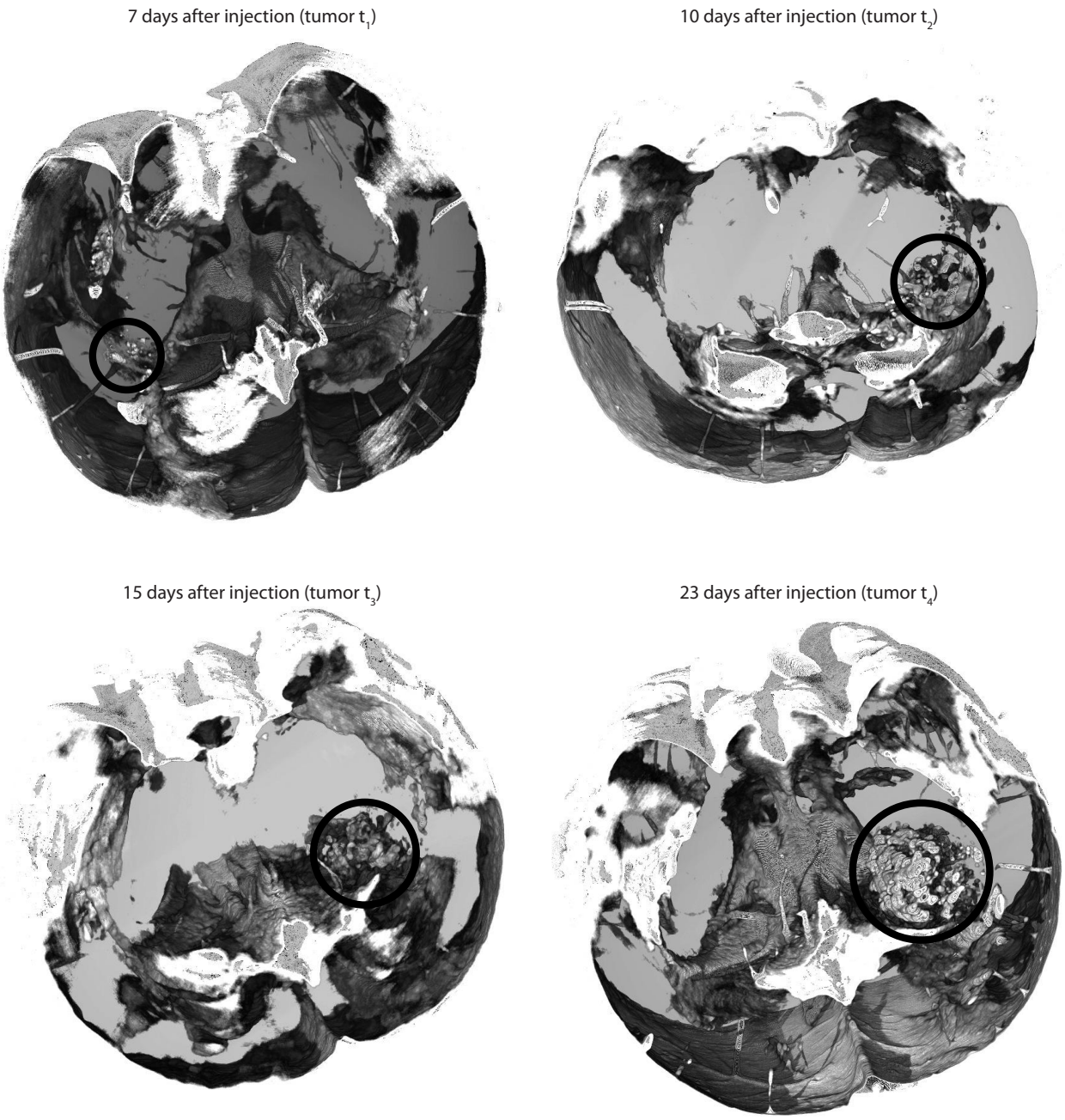

Figure 8. Three-dimensional renderings of the data sets after intensity-based segmentation. The black circles indicate the positions of the tumors at the four selected stages of growth.

homogeneous refractive indices, they become more and more chaotic, resulting in a dark region in the tumor t_4 (indicated by the dashed ellipse in the image bottom right) associated with the necrotic part. The dark dots within the tumors and healthy brain tissues (exemplary indicated by arrows) are identified as blood vessels.

3.2 Intensity-based segmentation of tumors

The electron density of the cancerous tissues shows lower values compared the healthy tissues, indicated by line plots and left shoulder in the histograms of Figs. 3, 4, 5 and 6. Therefore, an intensity-based segmentation of

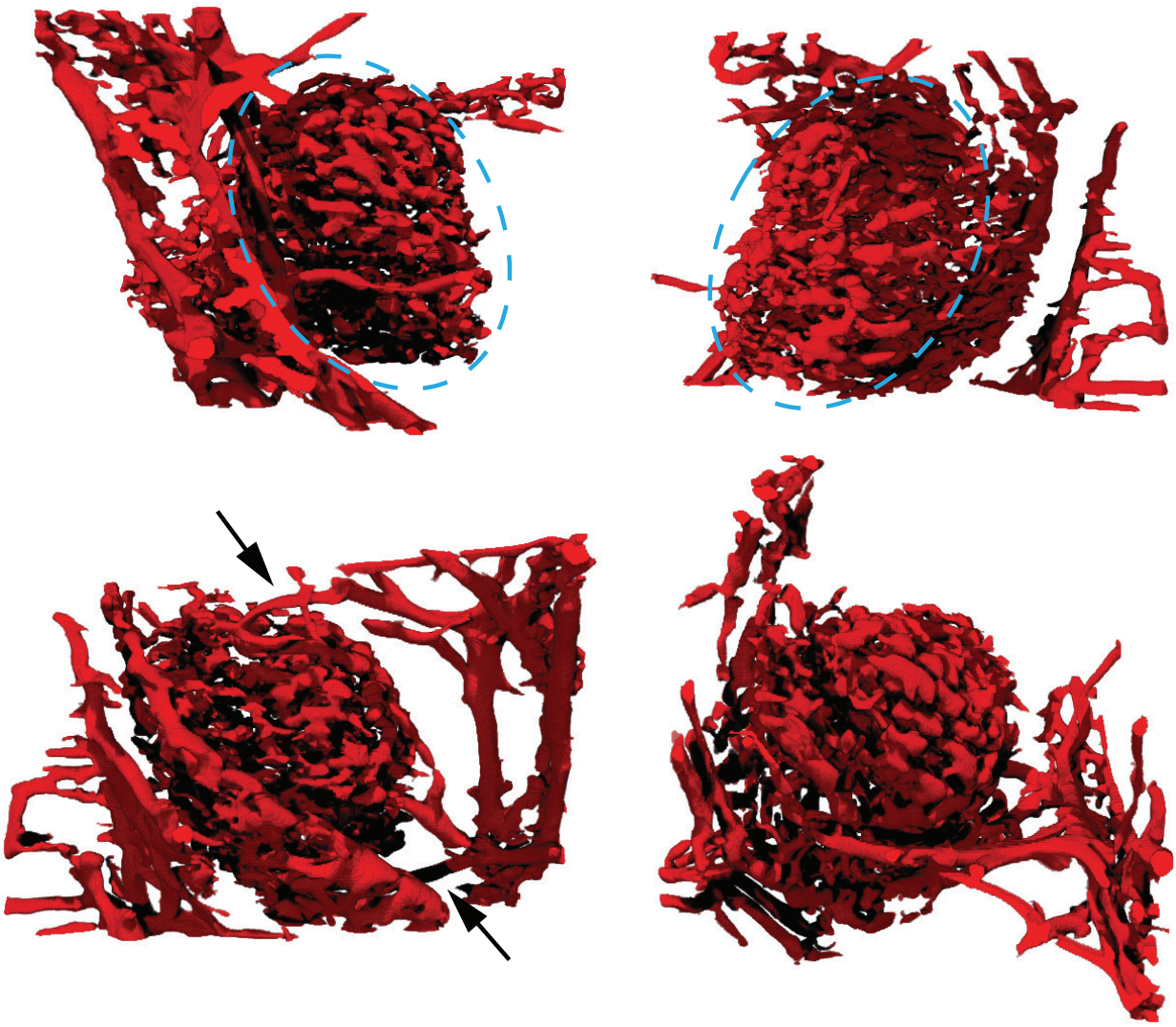

Figure 9. Three-dimensional renderings of tumor t_4 after the segmentation of the vessel tree. Light blue dashed ellipses (top row) show the position of the tumor. Black arrows (bottom left) direct to blood vessels located within the healhy tissue which are directly connected with the tumor.

the data sets was performed. Fig. 8 shows four renderings of the murine brains where the structure outside the gray values of the shoulder were made transparent. The tumors are highlighted by black circles. Besides the first brain, where the tumor is only hardly visible, this simple intensity-based segmentation allows us to visualize the tumors and some of the vessels of the surrounding healthy tissue.

3.3 Segmentation of vessel tree

Unfortunately, the simple segmentation in Fig. 8 fails for the discrimination of blood vessels in which we are interested. Only few larger blood vessels are visible in the 3D renderings but no smaller vessels are shown. Therefore a segmentation of the vessel tree of the cancerous part of the brain was performed using the VED algorithm (see Sec. 2.3). Fig. 9 shows the blood vessels of the tumor and the surrounded tissue of specimen t_4. Looking at these renderings of the blood vessels, one can easily separate the cancerous tissue from the healthy surrounded tissue. The dashed ellipses on top row of the figure highlight the cancerous part of the brain. Clearly, the vessel density inside the tumor is much higher than the density outside. Furthermore the blood vessels outside

look much more organized. The black arrows bottom left show two blood vessels of the healthy tissue which are connected to the tumorous part and which supply the tumor with blood. The blood vessels inside the tumor are organized very chaotic in comparison to the healthy tissue.

4. CONCLUSIONS

The vascular features including the average vessel diameter, number of bifurcations, average segment length or tortuosity will be determined for further analysis. This information can be used for the differentiation between angiogenic, necrotic and healthy regions of the brain and shows the hierarchy present in the vascular structure architecture (chaotic in the tumor vs. organized in the healthy part of the brain) [25]. We demonstrated that this technique can be used to succesfully visualize the vascular structure of brain tumor. This approach can be used to asses the efficacy of anti-angiogenic drugs targeting vessels as capillaries or larger arteries and veins. Here the efficacy of both components on different vessel sizes individually can be checked.

ACKNOWLEDGMENTS

The project was partially funded by Swiss National Science Foundation (project numbers: 200021_127297 and 200021_135496) and was supported by beam time from HASYLAB, DESY. This work was carried out with the support of the Karlsruhe Nano Micro Facility (KNMF, www.kit.edu/knmf), a Helmholtz Research Infrastructure at Karlsruhe Institute of Technology (KIT).

REFERENCES

[1] Rachet, B., Mitry, E., Quinn, M. J., N., C., and Coleman, M. P., "Survival from brain tumours in england and wales up to 2001," *Br. J. Cancer* **99**, S98–101 (2008).

[2] Omuro, A. and DeAngelis, L. M., "Glioblastoma and other malignant gliomas: a clinical review," *JAMA* **310**, 1842–1850 (2013).

[3] Werahera, P. N., Glode, L. M., La Rosa, F. G., Lucia, M. S., Crawford, E. D., Easterday, K., Sullivan, H. T., Sidhu, R. S., Genova, E., and Hedlund, T., "Proliferative Tumor Doubling Times of Prostatic Carcinoma," *Prostate Cancer* **2011**, 301850 (2011).

[4] Bergers, G. and Benjamin, L. E., "Angiogenesis: Tumorigenesis and the angiogenic switch," *Nat. Rev. Cancer* **3**, 401–410 (2003).

[5] Cea, V., Sala, C., and Verpelli, C., "Antiangiogenic therapy for glioma," *J. Sig. Transd.* **2012**, 483040 (2012).

[6] Lang, S., Müller, B., Dominietto, M. D., Cattin, P. C., Zanette, I., Weitkamp, T., and Hieber, S. E., "Three-dimensional quantification of capillary networks in healthy and cancerous tissues of two mice," *Microvasc. Res.* **84**, 314–322 (2012).

[7] Müller, B., Lang, S., Dominietto, M., Rudin, M., Schulz, G., Deyhle, H., Germann, M., Pfeiffer, F., David, C., and Weitkamp, T., "High-resolution tomographic imaging of microvessels ," *Proc. SPIE* **7078**, 70780B (2008).

[8] Fitzgerald, R., "Phase-sensitive X-ray imaging," *Phys. Today* **53**, 23–26 (2000).

[9] Schulz, G., Weitkamp, T., Zanette, I., Pfeiffer, F., Beckmann, F., David, C., Rutishauser, S., Reznikova, E., and Müller, B., "High-resolution tomographic imaging of a human cerebellum: Comparison of absorption and grating based phase contrast," *J. R. Soc. Interface* **7**, 1665–1676 (2010).

[10] David, C., Nöhammer, B., Solak, H. H., and Ziegler, E., "Differential X-ray phase contrast imaging using a shearing interferometer," *Appl. Phys. Lett.* **81**, 3287–3289 (2002).

[11] Momose, A., Kawamoto, S., Koyama, I., Hamaishi, Y., Takai, K., and Suzuki, Y., "Demonstration of X-ray Talbot interferometry," *Jpn. J. Appl. Phys., Part 2* **42**, 866–868 (2003).

[12] Weitkamp, T., David, C., Kottler, C., Bunk, O., and Pfeiffer, F., "Tomography with grating interferometers at low-brilliance sources," *Proc. SPIE* **6318**, 63180S (2006).

[13] Pfeiffer, F., Kottler, C., Bunk, O., and David, C., "Hard X-ray phase tomography with low-brilliance sources," *Phys. Rev. Lett.* **98**, 108105 (2007).

[14] Schulz, G., Crooijmans, H. J., Germann, M., Scheffler, K., Müller-Gerbl, M., and Müller, B., "Three-dimensional strain fields in human brain resulting from formalin fixation," *J. Neurosci. Methods* **202**, 17–27 (2011).

[15] Beckmann, F., Herzen, J., Haibel, A., Müller, B., and Schreyer, A., "High density resolution in synchrotron-radiation-based attenuation-contrast microtomography ," *Proc. SPIE* **7078**, 70781D (2008).

[16] Herzen, J., Donath, T., Beckmann, F., Ogurreck, M., David, C., Mohr, J., Pfeiffer, F., and Schreyer, A., "X-ray grating interferometer for materials-science imaging at a low-coherent wiggler source," *Rev. Sci. Instrum.* **82**, 113711 (2011).

[17] David, C., Bruder, J., Rohbeck, T., Grünzweig, C., Kottler, C., Diaz, A., Bunk, O., and Pfeiffer, F., "Fabrication of diffraction gratings for hard X-ray phase contrast imaging," *Microelectron. Eng.* **84**, 1172–1177 (2007).

[18] Reznikova, E., Mohr, J., Boerner, M., Nazmov, V., and Jakobs, P.-J., "Soft x-ray lithography of high aspect ratio SU8 submicron structures," *Microsyst. Technol.* **14**, 1683–1688 (2008).

[19] Thurner, P., Beckmann, F., and Müller, B., "An optimization procedure for spatial and density resolution in hard X-ray micro-computed tomography," *Nucl. Instrum. Methods Phys. Res., Sect. B* **225**, 599–603 (2004).

[20] Schulz, G., Weitkamp, T., Zanette, I., Pfeiffer, F., Müller-Gerbl, M., David, C., and Müller, B., "Asymmetric rotational axis reconstruction of grating-based X-ray phase contrast tomography of the human cerebellum," *Proc. SPIE* **8506**, 850609 (2012).

[21] Faris, G. W. and Byer, R. L., "Three-dimensional beam-deflection optical tomography of a supersonic jet," *Appl. Opt.* **27**, 5202–5212 (1988).

[22] Pfeiffer, F., Bunk, O., Kottler, C., and David, C., "Tomographic reconstruction of three-dimensional objects from hard X-ray differential phase contrast projection images," *Nucl. Instrum. Methods Phys. Res. Sect. A* **580**, 925–928 (2007).

[23] Manniesing, R. and Niessen, W. J., "Multiscale Vessel Enhancing Diffusion in CT Angiography Noise Filtering," in [*Information Processing in Medical Imaging, 19th International Conference, IMPI 2005*], Christensen, G. E. and Sonka, M., eds., Springer (2005).

[24] Manniesing, R., Viergever, M. A., and Niessen, W. J., "Vessel enhancing diffusion: A scale space representation of vessel structures," *Med. Image Anal.* **10**, 815–825 (2006).

[25] Müller, B., Lang, S., Beckmann, F., Dominietto, M., Rudin, M., Zanette, I., Weitkamp, T., Rack, A., and Hieber, S. E., "Comparing the micro-vascular structure of cancerous and healthy tissues," *Proc. SPIE* **8506**, 850607 (2012).